Chemical Science

ROYAL SOCIETY OF CHEMISTRY

EDGE ARTICLE

View Article Online
View Journal | View Issue

Cite this: *Chem. Sci.*, 2026, **17**, 5661

All publication charges for this article have been paid for by the Royal Society of Chemistry

Atomic-scale redox-potential-mediated engineering of 0D/2D Cu–Cu_2O/$MO_x(OH)_y$ heterojunctions for efficient nitrate electroreduction to ammonia

Tuo Zhang,†[a] Tianzhi Hao,†[a] Xiangyang Hou,[b] Yuhui Yin,[a] Guowen Hu,[a] Genping Meng,[a] Shihao Sun,[a] Hua Li*[a] and Baodui Wang*[a]

The precise construction of zero-dimensional/two-dimensional (0D/2D) heterojunctions is often hindered by interfacial lattice mismatches and uncontrolled phase transitions, limiting their efficacy in electrocatalysis. Herein, we report a widely applicable redox-potential-mediated strategy for the atomically defined fabrication of 0D/2D Cu–Cu_2O/$MO_x(OH)_y$ heterojunctions (M = Ni, Fe, Mn, Co, Cr). This approach leverages the inherent differences in standard reduction potentials between Cu and transition metals to drive selective oxidation and ultrasound-assisted hydrolysis of pre-synthesized CuM alloy nanoparticles. This process results *in situ* phase separation, forming epitaxially embedded Cu–Cu_2O nanoparticles within ultrathin $MO_x(OH)_y$ nanosheets. As a proof of concept, the Cu–Cu_2O/$Ni(OH)_2$ heterojunction exhibits exceptional performance in the electrocatalytic nitrate reduction reaction (eNITRR), achieving an outstanding ammonia yield rate of 12,974.5 μg cm^{-2} h^{-1} (at a mass loading of 1 mg cm^{-2}) and a Faradaic efficiency of 98.15%, ranking it among the high-performing catalysts reported to date. Mechanistic studies reveal a synergistic interfacial effect: Cu–Cu_2O promotes nitrate adsorption and activation, while $Ni(OH)_2$ selectively cleaves H_2O to generate reactive *H species, thereby accelerating the hydrogenation steps. This redox-guided synthesis provides a useful framework for the atomic-scale engineering of heterointerfaces, paving the way for advanced electrocatalysts in sustainable nitrogen valorization and beyond.

Received 18th November 2025
Accepted 22nd January 2026

DOI: 10.1039/d5sc08998k

rsc.li/chemical-science

Introduction

The rational design and precise synthesis of hetero-nanoarchitectures from structurally dissimilar building blocks represent a foundational challenge in materials chemistry.[1] Integrating zero-dimensional nanoparticles (0D NPs) with two-dimensional nanosheets (2D NSs) is a particularly compelling strategy, as such 0D/2D heterojunctions can combine the high surface activity of NPs with the exceptional charge transport and confinement effects of 2D matrices, often leading to emergent catalytic properties.[2–4] However, the bottom-up construction of these hybrid materials with atomic-level interfacial control is often hindered by lattice mismatches and uncontrolled phase transformations during synthesis, resulting in poorly defined interfaces that obscure fundamental structure–property relationships and limit catalytic performance.[5,6]

This synthetic challenge is acutely evident in the development of advanced electrocatalysts for complex, multi-step reactions such as the electrochemical nitrate reduction reaction (eNITRR). The conversion of nitrate (NO_3^-) pollutants to valuable ammonia (NH_3) presents a sustainable route for simultaneous wastewater remediation and chemical production.[7–9] Copper-based materials have shown exceptional promise for eNITRR, primarily due to the favorable alignment of their d-orbitals with nitrate orbitals, enabling strong adsorption and facile activation of NO_3^-.[9,10] Recent advances highlight that constructing Cu/Cu_2O heterointerfaces can further enhance performance by synergistically modulating the d-band center to optimize the adsorption energies of key intermediates.[11–13] Nevertheless, the complete conversion of NO_3^- to NH_3 involves a complex, multi-step hydrogenation pathway that requires a continuous and efficient supply of active hydrogen atoms (*H), typically sourced from water dissociation.[14–18] Conventional Cu-based catalysts, while effective for nitrate activation, generally exhibit limited efficiency in cleaving the H–OH bond, creating a critical bottleneck in the proton-coupled electron transfer processes and ultimately restricting the overall NH_3 production rate.[7,8,19]

[a]State Key Laboratory of Natural Product Chemistry, College of Chemistry and Chemical Engineering, Lanzhou University, Lanzhou 730000, Gansu, China. E-mail: huali@lzu.edu.cn; wangbd@lzu.edu.cn

[b]Department of Chemistry and Biochemistry, Florida International University, USA

† These authors contributed equally to this work.

A potential solution lies in the strategic design of heterojunctions that couple distinct active sites, one for nitrate adsorption/activation and another for efficient water dissociation and *H generation. In this context, 2D transition metal hydroxides ($MO_x(OH)_y$) have recently emerged as exceptional platforms for activating water molecules and generating *H species.[20–23] Their ultrathin nature provides abundant unsaturated coordination sites and facilitates rapid interfacial charge transfer. Consequently, the integration of 0D Cu-based NPs with 2D $MO_x(OH)_y$ NSs is a highly promising avenue for creating synergistic catalysts. However, the realization of such precisely controlled 0D/2D architectures remains a formidable synthetic challenge. Conventional methods often fail to achieve epitaxial integration or control interfacial redox chemistry, leading to incoherent interfaces and suboptimal catalytic synergy.[24,25]

Herein, we propose and demonstrate that the inherent standard reduction potentials (E^0) of constituent metals can serve as a powerful, predictive descriptor to guide the precise synthesis of 0D/2D heterojunctions. We present a general redox-potential-mediated strategy for fabricating a class of atomically defined Cu–Cu_2O/$MO_x(OH)_y$ (M = Ni, Fe, Mn, Co, Cr) heterostructures. The core of our approach lies in exploiting the thermodynamic disparity in standard reduction potentials between copper ($E^0(Cu^{2+}/Cu^0)$ = +0.34 V) and various first-row transition metals, including nickel ($E^0(Ni^{2+}/Ni^0)$ = −0.25 V), iron ($E^0(Fe^{2+}/Fe^0)$ = −0.44 V), manganese ($E^0(Mn^{2+}/Mn^0)$ = −1.18 V), cobalt ($E^0(Co^{2+}/Co^0)$ = −0.28 V), and chromium ($E^0(Cr^{3+}/Cr^0)$ = −0.74 V). Starting from pre-synthesized CuM alloy NPs, controlled oxidation and ultrasound-assisted hydrolysis selectively leach and transform the more oxidizable metal M into ultrathin $MO_x(OH)_y$ NSs, while Cu undergoes controlled oxidation to form epitaxially embedded Cu–Cu_2O NPs. As a compelling proof-of-concept, the optimal Cu–Cu_2O/$Ni(OH)_2$ heterojunction exhibits an exceptional Faradaic efficiency of 98.15% and a record-high ammonia yield rate of 12,974.5 μg cm^{-2} h^{-1}. Through a combination of *in situ* spectroscopic techniques and density functional theory (DFT) calculations, we decipher the interfacial synergy: Cu–Cu_2O acts as the primary site for nitrate adsorption and activation, while $Ni(OH)_2$ efficiently dissociates water to supply *H species, collectively accelerating the hydrogenation steps. This work establishes a widely applicable paradigm for using fundamental

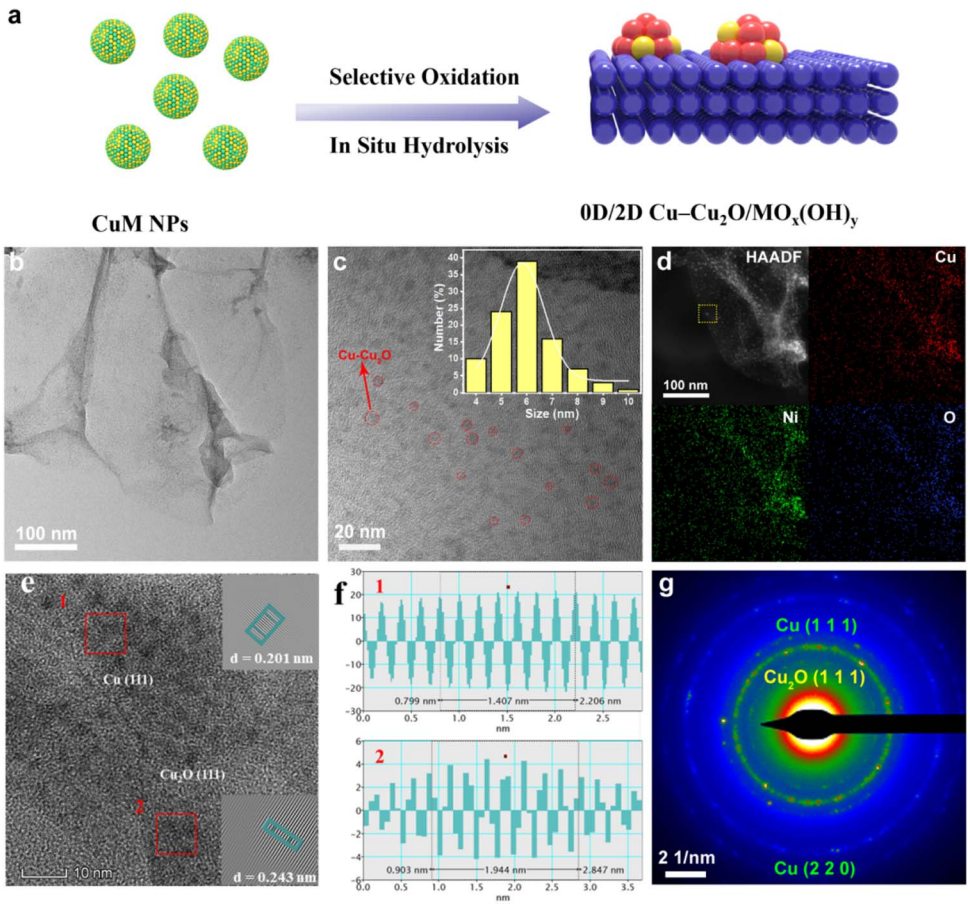

Fig. 1 Synthesis and morphological characterization of Cu–Cu_2O/$Ni(OH)_2$. (a) Schematic illustration of the redox-potential-mediated synthesis of Cu–Cu_2O/$MO_x(OH)_y$ heterojunctions. (b) TEM image of the as-synthesized Cu–Cu_2O/$Ni(OH)_2$. (c) High-resolution TEM (HR-TEM) image and the corresponding particle size distribution of Cu–Cu_2O NPs. (d) HAADF-STEM image and corresponding elemental mapping for Cu, Ni, and O. (e) HR-TEM image showing lattice fringes of different crystalline domains; insets are magnified FFT-filtered images of regions 1 and 2. (f) Corresponding lattice spacing analysis of regions 1 and 2 marked in (e). (g) SAED pattern of Cu–Cu_2O/$Ni(OH)_2$.

electrochemical properties to navigate the precision synthesis of complex functional materials, with implications that extend well beyond electrocatalysis.

Results and discussion

Synthesis and structural characterization

The Cu–Cu_2O/$MO_x(OH)_y$ heterojunction was synthesized *via* a three-step redox-potential-mediated process, which capitalizes on the distinct standard reduction potentials of Cu and transition metal M to achieve selective oxidation and phase separation. As illustrated in Fig. 1a, the process involves: (1) liquid-phase reduction of Cu-oleate and M-oleate complexes using sodium borohydride at ambient temperature to form CuM alloy nanoparticles (NPs); (2) selective oxidation of the as-synthesized CuM NPs under controlled conditions; and (3) ultrasound-assisted hydrolysis to promote the *in situ* growth of two-dimensional $MO_x(OH)_y$ nanosheets (NSs). The resulting CuM NPs were characterized by typical transmission electron microscopy (TEM) (Fig. S1, SI), X-ray powder diffraction (XRD) (Fig. S2, SI). The ultrasound treatment not only provides the energy for hydrolysis and exfoliation but also enhances mass transfer, facilitating the formation of ultrathin NSs. Specifically, when CuNi NPs are subjected to ultrasound in deionized water, the Ni component ($E^0(Ni^{2+}/Ni^0) = -0.25$ V) is preferentially oxidized and hydrolyzed to form ultrathin $Ni(OH)_2$ NSs (Fig. 1b), while the Cu ($E^0(Cu^{2+}/Cu^0) = +0.34$ V) undergoes partial oxidation to form Cu–Cu_2O NPs anchored on the $Ni(OH)_2$ substrate (Fig. 1c). TEM analysis confirms the two-dimensional sheet-like morphology of $Ni(OH)_2$ and the homogeneous dispersion of Cu–Cu_2O NPs with an average size of 5.9 nm on the NSs. The formation of heterojunction interfaces between Cu and Cu_2O NPs is also clearly observed (Fig. S3, SI). Elemental mapping *via* high-angle annular dark-field scanning transmission electron microscopy (HAADF-STEM) (Fig. 1d) confirms the uniform distribution of Cu, Ni, and O throughout the structure. High-resolution TEM (HR-TEM) images (Fig. 1e and f) reveal lattice fringes corresponding to Cu (111) (0.201 nm) and Cu_2O (111) (0.243 nm), with insets showing magnified FFT-filtered images of regions 1 and 2. The selected-area electron diffraction (SAED) pattern (Fig. 1g) further confirms the coexistence of Cu and Cu_2O crystalline phases, providing clear evidence for the successful construction of the Cu–Cu_2O/$Ni(OH)_2$ heterojunction *via* the redox-mediated strategy.

Crystalline phase and valence state analysis

XRD analysis reveals the coexistence of metallic Cu and Cu_2O crystalline phases in the synthesized material (Fig. 2a), validating the spontaneous growth of Cu–Cu_2O NPs on $Ni(OH)_2$ nanosheets. The diffraction peaks at 43.47° and 50.37° are assigned to the (111) and (200) planes of cubic Cu (JCPDS No. 04-0836), while peaks at 29.54°, 36.42°, 42.30°, and 61.34° correspond to the (110), (111), (200), and (220) planes of cubic Cu_2O (JCPDS No. 65-3288).[26] The absence of discernible diffraction peaks for $Ni(OH)_2$ suggests its amorphous nature.[27] The surface chemical states of the Cu–Cu_2O/$Ni(OH)_2$ heterojunction were determined by XPS. The Cu 2p spectrum (Fig. 2b) exhibited peaks at binding energies of 930.47 eV and 950.27 eV, indicative of $Cu^{0/1+}$ species.[28–30] The peak at ~932.31 eV can be attributed to residual surface copper-oleate species. In the Ni 2p spectrum (Fig. 2c), the peaks at 852.68 eV and 871.94 eV are characteristic of Ni^{2+} species,[31] with satellite peaks observed at higher binding energies.[32,33] Auger electron spectroscopy (AES) analysis provided further insight into the copper oxidation states. The peaks at 568 eV and 570.5 eV corresponded to Cu^0 and Cu^+, with relative abundances of 22.45% and 77.55%, respectively (Fig. 2d), indicating that copper predominantly exists in the +1 oxidation state.[34] Cu K-edge XANES analysis (Fig. 2e) corroborated these findings. The absorption edge position and spectral shape closely resembled that of the Cu_2O reference, indicating Cu^+ as the predominant species. A linear correlation between absorption edge energy and formal valence state (Fig. 2f) yielded an average Cu oxidation state of approximately +0.78, consistent with the XPS and AES results. In summary, combined characterization by XRD, XPS, AES, and XANES consistently demonstrates that copper in the composite is primarily in the Cu^+ state, with a minor contribution from Cu^0, a distribution favorable for interfacial electron transfer and catalytic selectivity.

Formation pathway and structural evolution

To elucidate the formation mechanism of the Cu–Cu_2O/$Ni(OH)_2$ heterojunction, we monitored the structural evolution during ultrasonic treatment (Fig. 3a). TEM images (Fig. 3b–e and S4, SI) and time-dependent XRD spectra (Fig. 3f and S5, SI) track the transformation. Initially, Ni within the CuNi alloy NPs is preferentially oxidized and hydrolyzed to form $Ni(OH)_2$ NSs, which become thinner with prolonged ultrasonication. Concurrently, Cu is oxidized to form Cu–Cu_2O NPs that deposit onto the growing NSs. The XRD peaks corresponding to the CuNi alloy (*e.g.*, at 43.1°) diminish, while those for Cu (43.3°) and Cu_2O (36.42°, 61.52°) emerge and intensify. No metallic Ni peaks are observed, confirming the complete hydrolysis of Ni. Both TEM and XRD confirm the redox-driven phase separation, resulting in well-defined 0D/2D heterojunctions. The relative content of copper and nickel remains stable throughout the process (Table S1), indicating a conservative transformation.

Extension to other metal systems: widely applicable synthesis strategy

To demonstrate the wide applicability of our redox-potential-mediated strategy, we synthesized Cu–Cu_2O/$MO_x(OH)_y$ heterojunctions through the simple introduction of the corresponding as-synthesized CuM NPs (M = Cr, Mn, Fe, and Co). XRD analysis (Fig. S6, SI) confirmed the coexistence of Cu and Cu_2O phases in all cases. XPS (Fig. S7, SI), AES (Fig. S8, SI), and M 2p spectra (Fig. S9, SI) indicated that the introduction of different M elements had a minimal impact on the oxidation state of Cu, further validating the robustness of our method. The hydrolysis of metal M led to the formation of the respective $MO_x(OH)_y$, as evidenced by their corresponding lattice fringes (Fig. S10, SI).

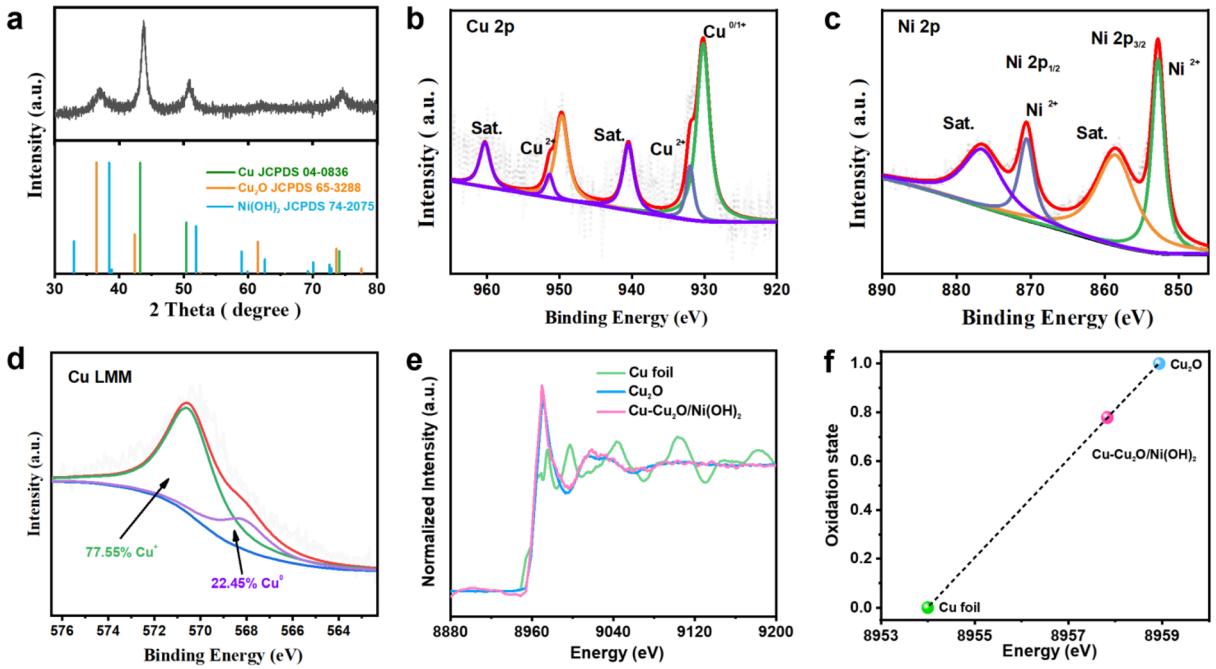

Fig. 2 Crystalline phase and valence state of Cu–Cu_2O/$Ni(OH)_2$. (a) XRD pattern of Cu–Cu_2O/$Ni(OH)_2$. (b) High-resolution XPS spectrum of Cu 2p. (c) High-resolution XPS spectrum of Ni 2p. (d) Cu LMM Auger electron spectrum. (e) Cu K-edge XANES spectra of Cu foil, Cu_2O, and Cu–Cu_2O/$Ni(OH)_2$. (f) Correlation between absorption edge energy and the oxidation state of Cu species.

TEM analysis (Fig. 4) revealed the particle size distribution of Cu–Cu_2O NPs grown on various $MO_x(OH)_y$ NSs. Cu–Cu_2O/CrOOH exhibited the smallest Cu–Cu_2O particle size (2.38 nm), followed by Cu–Cu_2O/FeOOH (3.10 nm), Cu–Cu_2O/$Co(OH)_2$ (4.29 nm), and Cu–Cu_2O/$Mn(OH)_2$ (4.40 nm). This trend suggests that CrOOH most effectively restricts copper particle nucleation and growth, while $Mn(OH)_2$ and $Co(OH)_2$ exert a weaker influence. EDS mapping confirmed the uniform distribution of Cr, Mn, Fe, and Co elements in their respective samples. HR-TEM analysis revealed variations in lattice spacings: Cu_2O(111) spacings were similar for Cu–Cu_2O/CrOOH and Cu–Cu_2O/FeOOH (~0.241 nm), while Cu–Cu_2O/$Mn(OH)_2$ exhibited the largest spacing (0.249 nm). For Cu(111), spacings ranged from 0.208 nm (Cu–Cu_2O/CrOOH, Cu–Cu_2O/$Mn(OH)_2$) to 0.216 nm (Cu–Cu_2O/$Co(OH)_2$). These results underscore the crucial role of the M element and ultrasound in regulating the final structure of the Cu-based heterojunction catalysts, highlighting the method's versatility.

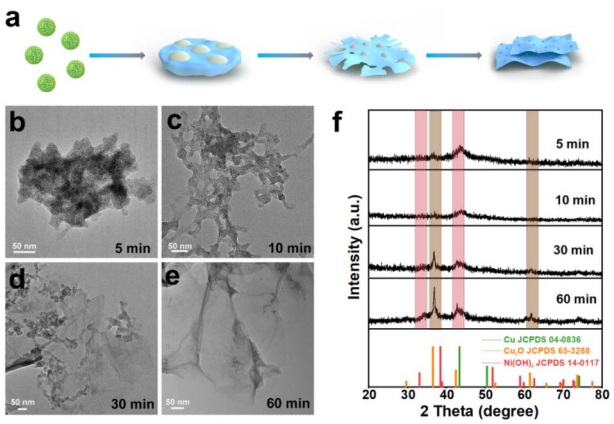

Fig. 3 Formation pathway and structural evolution of Cu–Cu_2O/$Ni(OH)_2$. (a) Schematic illustration of the formation process. (b–e) TEM images of CuNi nanoparticles subjected to ultrasound for different durations. (f) XRD patterns tracking the phase transformation during ultrasonic treatment.

Electrocatalytic nitrate reduction performance

The electrochemical nitrate reduction reaction (eNITRR) performance of the catalysts and carbon felt was evaluated in a standard three-electrode H-type cell. Control samples, including $Ni(OH)_2$ NSs, Cu–Cu_2O NPs, and a physical mixture of Cu–Cu_2O + $Ni(OH)_2$, were synthesized and characterized (Fig. S11, S12, SI). Product concentrations (NO_3^-, NO_2^-, NH_3) were quantified using colorimetric methods (Fig. S13–S15) and ion chromatography (IC) (Fig. S16, S17, SI).

For each sample, linear sweep voltammetry (LSV) curves were acquired to confirm the current density (j) of the reaction (Fig. 5a). The LSV curves were recorded after 5 cycles sweeping between the potential from −0.49 V to 1.01 V (*vs.* RHE). As shown in Fig. 5a, in the presence of NO_3^-, with the exception of carbon felt and $Ni(OH)_2$ NSs, the j of other catalysts significantly increases as the reduction overpotential increases. At the same potential, the Cu–Cu_2O/$Ni(OH)_2$ catalyst exhibits the highest j, indicating its superior electrocatalytic nitrate reduction activity. Fig. 5b shows the Tafel slope plots for $Ni(OH)_2$, CuNi NPs, Cu–Cu_2O, Cu–Cu_2O + $Ni(OH)_2$, and Cu–Cu_2O/$Ni(OH)_2$, where Cu–Cu_2O/$Ni(OH)_2$ demonstrates a Tafel slope of 106.82 mV dec^{-1}, signifying its lowest overpotential and more favorable kinetics for the eNITRR. The Cu–Cu_2O/$Ni(OH)_2$ heterojunction exhibits

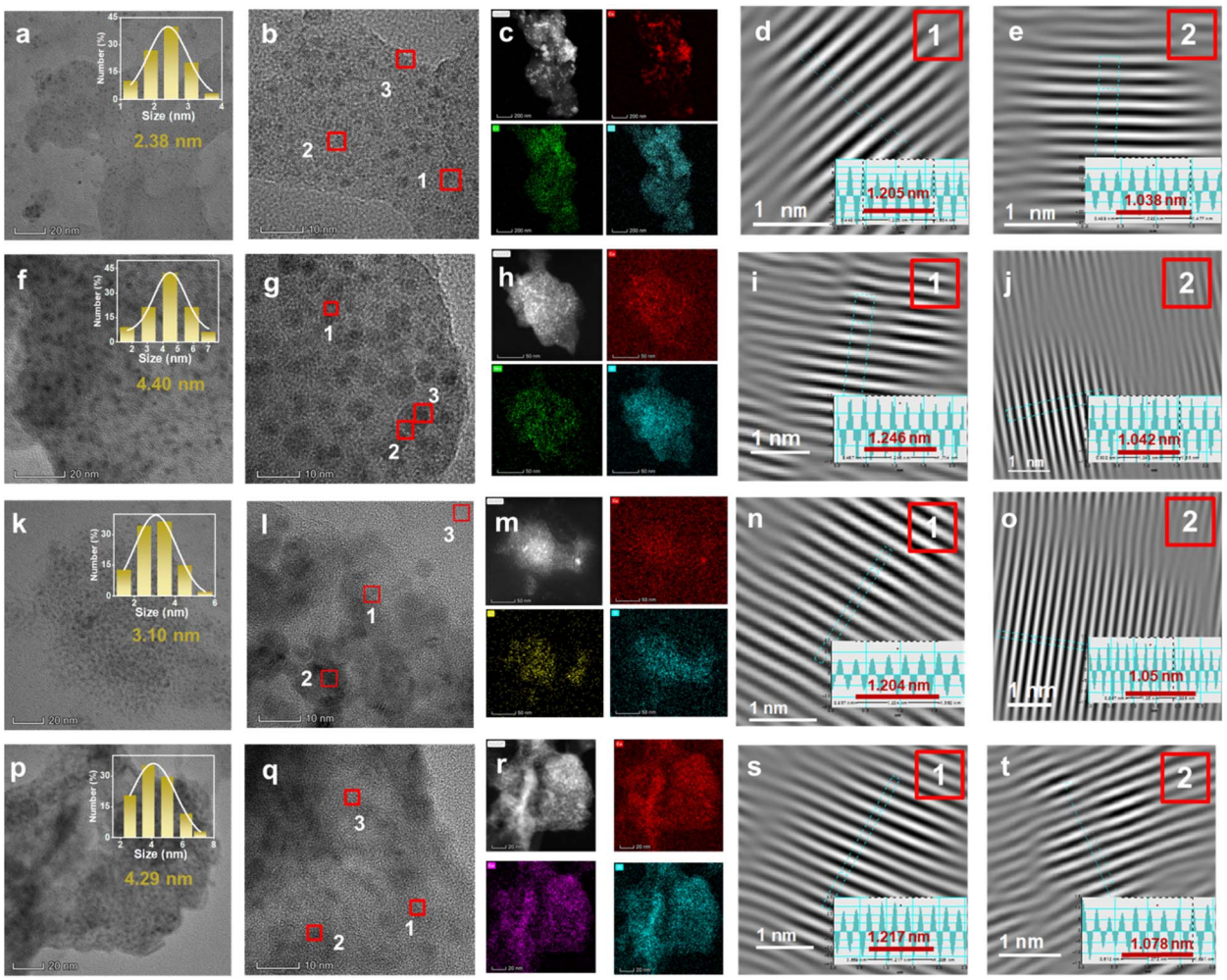

Fig. 4 TEM images of four different materials, arranged side by side, provide multilayered information for each material. (a) Low-magnification TEM image, (b) HR-TEM image, (c) HAADF-STEM image and corresponding elemental mapping, (d) Cu_2O (111) crystal plane at position 1 with a lattice spacing of 0.241 nm, and (e) Cu (111) crystal plane at position 2 with a lattice spacing of 0.208 nm, for Cu–Cu_2O/CrOOH. (f) Low-magnification TEM image, (g) HR-TEM image, (h) HAADF-STEM image and corresponding elemental mapping, (i) Cu_2O (111) crystal plane at position 1 with a lattice spacing of 0.249 nm, and (j) Cu (111) crystal plane at position 2 with a lattice spacing of 0.208 nm, for Cu–Cu_2O/$Mn(OH)_2$. (k) Low-magnification TEM image, (l) HR-TEM image, (m) HAADF-STEM image and corresponding elemental mapping, (n) Cu_2O (111) crystal plane at position 1 with a lattice spacing of 0.241 nm, and (o) Cu (111) crystal plane at position 2 with a lattice spacing of 0.210 nm, for Cu–Cu_2O/FeOOH. (p) Low-magnification TEM image, (q) HR-TEM image, (r) HAADF-STEM image and corresponding elemental mapping, (s) Cu_2O (111) crystal plane at position 1 with a lattice spacing of 0.243 nm, and (t) Cu (111) crystal plane at position 2 with a lattice spacing of 0.216 nm, for Cu–Cu_2O/$Co(OH)_2$. The second column highlights regions 1, 2, and 3 for detailed crystal analysis, corresponding to the Cu_2O (111) crystal plane, Cu (111) crystal plane, and $MO_x(OH)_y$, respectively.

the smallest semicircle diameter in the Nyquist plot (Fig. S22a, SI), indicating the lowest charge-transfer resistance among the three catalysts and thus the most favorable reaction kinetics. Fig. S22c (SI) shows that the local pH at the Cu–Cu_2O/$Ni(OH)_2$ electrode surface gradually increases during the reaction, indicating interfacial alkalization caused by continuous proton consumption in electrochemical nitrate reduction. In Fig. 5c, a Faradaic efficiency (FE) comparison is presented for $Ni(OH)_2$, CuNi NPs, Cu–Cu_2O, Cu–Cu_2O + $Ni(OH)_2$, and Cu–Cu_2O/$Ni(OH)_2$ catalysts in the NH_3 production process. The FE of Cu–Cu_2O/$Ni(OH)_2$ is 98.15%, significantly surpassing that of $Ni(OH)_2$ (64.85%), CuNi NPs (69.50%), Cu–Cu_2O (48.58%) and Cu–Cu_2O + $Ni(OH)_2$ (53.30%). Additionally, the NH_3 yield of Cu–Cu_2O/$Ni(OH)_2$ is notably higher than that of $Ni(OH)_2$ and Cu–Cu_2O. Fig. 5d shows the change of mass normalized selectivity of NO_2^- and NH_4^+ on Cu–Cu_2O and Cu–Cu_2O/$Ni(OH)_2$ over time at a low overpotential (0.01 V *vs.* RHE). During the reaction, Cu–Cu_2O generates a significant amount of harmful intermediate NO_2^- products. However, on the Cu–Cu_2O/$Ni(OH)_2$ catalyst, the selectivity of NO_2^- decreases over time while the selectivity of NH_3 increases. After 24 h, the selectivity of NH_3 reaches 98.5%, whereas the selectivity of NO_2^- is only 1.5%. The outstanding eNITRR performance of Cu–Cu_2O/$Ni(OH)_2$ can be attributed to the synergistic effect at the interface of Cu–Cu_2O NPs and 2D $Ni(OH)_2$ NSs, in which NO_3^- is rapidly converted to NO_2^- by Cu–Cu_2O NPs and subsequently reduced to NH_4^+ by *H produced from activated water in $Ni(OH)_2$ NSs. Fig. 5e shows the change of NO_3^-–N, NH_4^+-N, and NO_2^--N concentrations with reaction

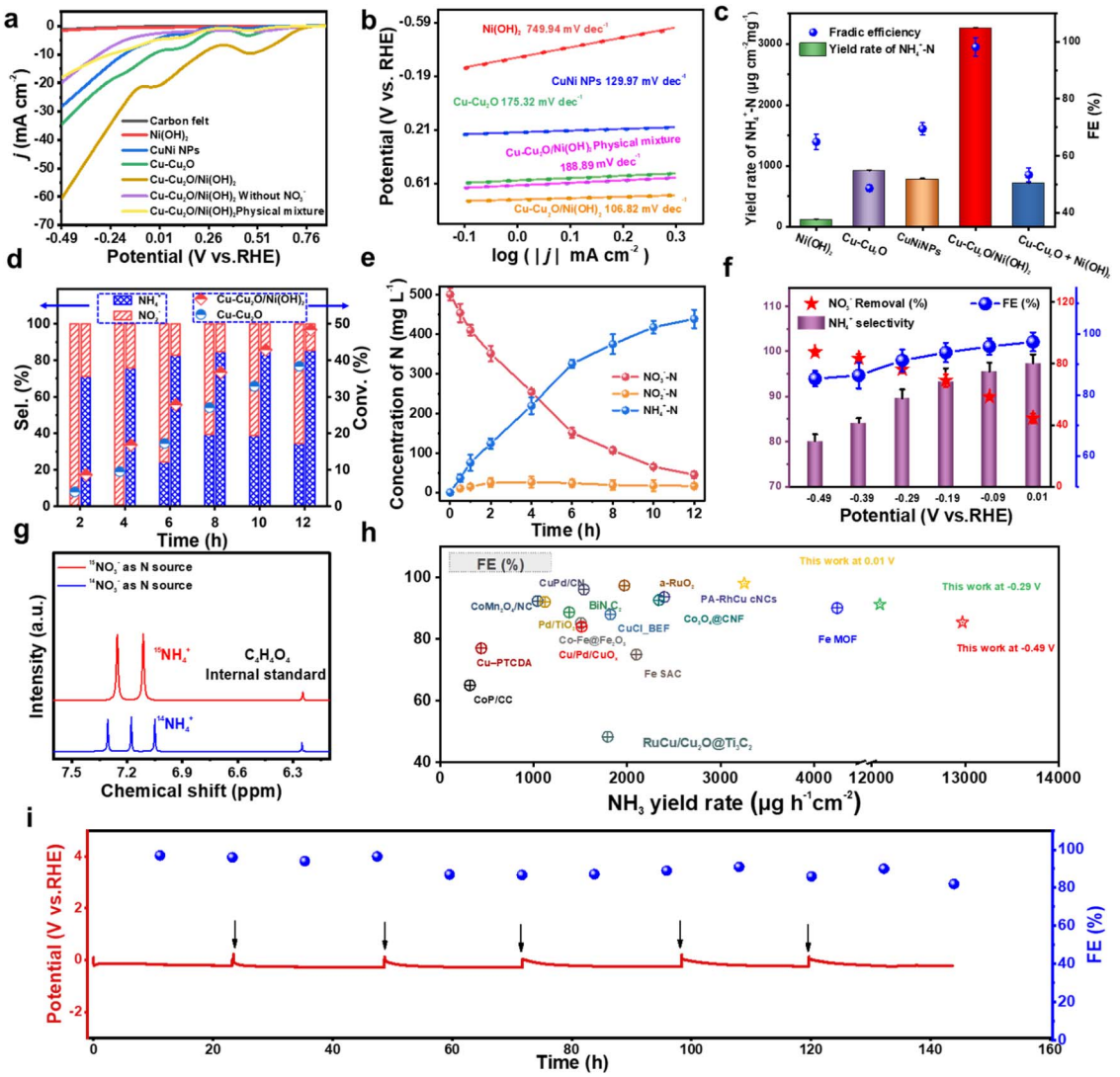

Fig. 5 eNITRR performance of different electrocatalyst. (a) *j*-V plots of electrocatalytic reduction of nitrate over carbon felt, $Ni(OH)_2$, CuNi NPs, Cu–Cu_2O, Cu–Cu_2O + $Ni(OH)_2$ and Cu–Cu_2O/$Ni(OH)_2$ heterojunctions (80% iR corrected). (b) Tafel slopes for $Ni(OH)_2$, CuNi NPs, Cu–Cu_2O, Cu–Cu_2O + $Ni(OH)_2$ and Cu–Cu_2O/$Ni(OH)_2$ catalysts. (c) Faradaic efficiency and yield of NH_4^+-N over $Ni(OH)_2$, CuNi NPs, Cu–Cu_2O, Cu–Cu_2O + $Ni(OH)_2$ and Cu–Cu_2O/$Ni(OH)_2$ catalysts. (d) Mass-normalized selectivity of NO_2^- and NH_4^+ over Cu–Cu_2O and Cu–Cu_2O/$Ni(OH)_2$ catalysts at 0.01 V (*vs.*RHE),1 g L^{-1} NO_3^--N as a function of reaction time. (e) NO_3^--N consumption, NO_2^--N generation, and NH_4^+-N generation over Cu–Cu_2O/$Ni(OH)_2$ catalysts at different times with 500 mg L^{-1} NO_3^--N. (f) NH_4^+ selectivity, NO_3^- removal rate and Faradaic efficiency of Cu–Cu_2O/$Ni(OH)_2$ catalysts at different potentials. (g) Detection of $^{14}NH_4^+$ and isotopically labeled $^{15}NH_4^+$ by ^1H NMR. (h) Comparison of the eNITRR performance of the Cu–Cu_2O/$Ni(OH)_2$ with other catalysts reported in the literature. (i) The long-term electrocatalytic stability of eNITRR on Cu–Cu_2O/$Ni(OH)_2$ was evaluated in an H-type cell at a current density of 20 mA cm^{-2}. The black arrows indicate the replenishment of fresh electrolytes.

time at a working potential of −0.49 V, and the initial NO_3^--N concentration is set at 500 mg L^{-1}. As the reaction time increases, the concentration of NO_3^--N continues to decrease while that of NH_4^+–N continues to increase; however, the concentration level remains relatively low for NO_2^-N, indicating the remarkable selectivity of the Cu–Cu_2O/$Ni(OH)_2$ catalyst in reducing NO_3^- to NH_4^+ with minimal generation of the byproduct NO_2^-. The electrochemical active surface area (ECSA) of different materials was also tested, and the experimental results show that Cu–Cu_2O/$Ni(OH)_2$ has the highest ECSA, suggesting it has the largest contact area with reactants, as shown in Fig. S18 (SI).

In order to further investigate the catalytic performance of the Cu–Cu_2O/$Ni(OH)_2$ catalyst, the removal rate of NO_3^-, selectivity for NH_4^+, and FE were measured at different potentials. As depicted in Fig. 5f, both NH_4^+ selectivity and FE gradually decrease with a reduction in potential due to increased generation of NO_2^- and competitive HER at lower potentials. Conversely, the NO_3^- removal rate increases gradually with decreasing potential as more energy is utilized for the electrocatalytic nitrate reduction process at low potential. Furthermore, the catalytic performance of Cu–Cu_2O/$Ni(OH)_2$ under different pH conditions (Fig. S22b, SI) shows that both the NH_3 yield and Faradaic efficiency (FE) initially increase and then

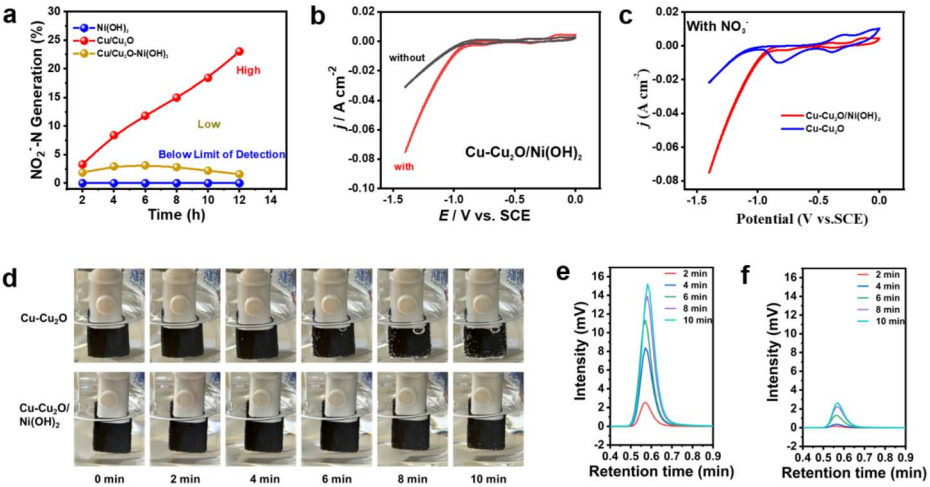

Fig. 6 Electrochemical methods for mechanistic investigation. (a) NO_2^- generation as a function of time over $Ni(OH)_2$ (Below Limit of detection), Cu–Cu_2O (High) and Cu–Cu_2O/$Ni(OH)_2$ (Low) (b) CV measurements of Cu/Cu_2O–$Ni(OH)_2$ with (red line) and without (black line) nitrate in 0.1 M NaOH solution and 500 mg L^{-1} NO_3^--N with 100 mV s^{-1} sweeping speed. (c) CV measurements of Cu–Cu_2O and Cu/Cu_2O–$Ni(OH)_2$ in 500 mg L^{-1} NO_3^--N solution with 100 mV s^{-1} sweeping speed. The CV curves were recorded after 5 cycles of surface cleaning. (d) Digital photographs of hydrogen precipitation from cathodes in the presence of NO_3^- at a potential of −0.49 V (*vs.*RHE). (e) The Cu–Cu_2O and (f) Cu–Cu_2O/$Ni(OH)_2$ catalyzed H_2 generation curves in the presence of NO_3^-.

decrease with increasing electrolyte pH, indicating that moderately alkaline conditions favor nitrate reduction, whereas excessive alkalinity may limit proton availability. In addition, as shown in Fig. S22d (SI), the NH_3 yield increases with nitrate concentration, while the FE exhibits a volcano-type dependence, suggesting that although higher nitrate concentrations enhance reaction rates, mass-transport limitations reduce electron utilization efficiency at high concentrations. The ammonia origin was determined through ^{15}N isotope labeling experiments. As shown in Fig. 5g and S19 (SI), utilization of $Na^{14}NO_3$ as the nitrogen source in the electrolyte resulted in three characteristic $^{14}NH_4^+$ peaks at chemical shifts of 6.91 ppm, 7.04 ppm, and 7.17 ppm in the post-reaction electrolyte's ^1H NMR spectrum. Conversely, when $Na^{15}NO_3$ was employed as the nitrate source, the resulting ^1H NMR spectra exhibited distinct double peaks corresponding to $^{15}NH_4^+$ at chemical shifts of 6.95 ppm and 7.13 ppm with no additional peaks present, confirming that the obtained $^{15}NH_4^+$ originated solely from electrochemical reduction of $Na^{15}NO_3$ in presence of catalyst rather than environmental contamination.[35] In comparison to the majority of reported electrocatalytic nitrate reduction catalysts, the Cu–Cu_2O/$Ni(OH)_2$ catalyst exhibits superior NH_3 production rate and Faradaic efficiency at different potentials (Fig. 5h and Table S2). Furthermore, Cu–Cu_2O/$Ni(OH)_2$ exhibited excellent electrochemical stability, maintaining long-term stability for over 140 hours at a current density of 20 mA cm^{-2}, with negligible decay in activity and Faradaic efficiency (Fig. 5i and S20, SI). This demonstrates the strong application potential of Cu–Cu_2O/$Ni(OH)_2$ in electrolytic systems.[36] After XRD, TEM, and XPS characterization analyses (Fig. S23, SI), a gradual conversion of partial Cu_2O to metallic Cu was observed in Cu–Cu_2O/$Ni(OH)_2$ during the cyclic electrocatalytic process.[37] In addition, during the catalytic process, the morphology of the Cu–Cu_2O/$Ni(OH)_2$ catalyst did not undergo any significant changes. This indicates that the Cu–Cu_2O/$Ni(OH)_2$ catalyst can maintain its structural and morphological stability during the reaction process, ensuring the continuity and reliability of its catalytic activity.

Mechanistic insights from synergistic interface effects

To further elucidate the mechanism of Cu–Cu_2O/$Ni(OH)_2$ electrocatalytic nitrate reduction, a series of electrochemical tests were conducted. Fig. 6a shows the time-dependent production of NO_2^- by $Ni(OH)_2$, Cu–Cu_2O and Cu–Cu_2O/$Ni(OH)_2$. It is evident that Cu–Cu_2O catalysis yields the highest amount of NO_2^-, while $Ni(OH)_2$ catalysis shows minimal production. In the case of Cu–Cu_2O/$Ni(OH)_2$, only a small quantity of NO_2^- is generated initially, followed by a gradual decrease over time. The cyclic voltammetry (CV) curves of Cu–Cu_2O/$Ni(OH)_2$ in the solution with and without NO_3^- are compared in Fig. 6b. The presence of NO_3^- induces conspicuous enhancement of cathodic current density beginning at ~0.01 V (*vs.* RHE) (red curve), confirming the reduction activity of NO_3^- at Cu–Cu_2O/$Ni(OH)_2$. As a poignant example, the CVs of Cu–Cu_2O and Cu–Cu_2O/$Ni(OH)_2$ in NO_3^- solution were acquired, shown in Fig. 6c. A clear difference is observed that the cathodic current density rises more quickly at Cu–Cu_2O/$Ni(OH)_2$ than at Cu–Cu_2O after ~0.01 V (*vs.* RHE), highlighting the outstanding catalytic capability of Cu–Cu_2O/$Ni(OH)_2$ on NO_3^- reduction under the studying conditions.[38] These control experiments suggest that the introduction of $Ni(OH)_2$ to the catalyst system remarkably promotes its catalytic performance. The rapid consumption of *H by NO_2^- is beneficial to improve FE, otherwise, the accumulation of *H is prone to forming hydrogen gas.[39] The existing study pointed out that under the HER process at low overpotential (close to equilibrium potential), the reaction rates of HER and hydrogen oxidation reaction (HOR) are nearly comparable ($i_{HER} \approx i_{HOR}$) so that the

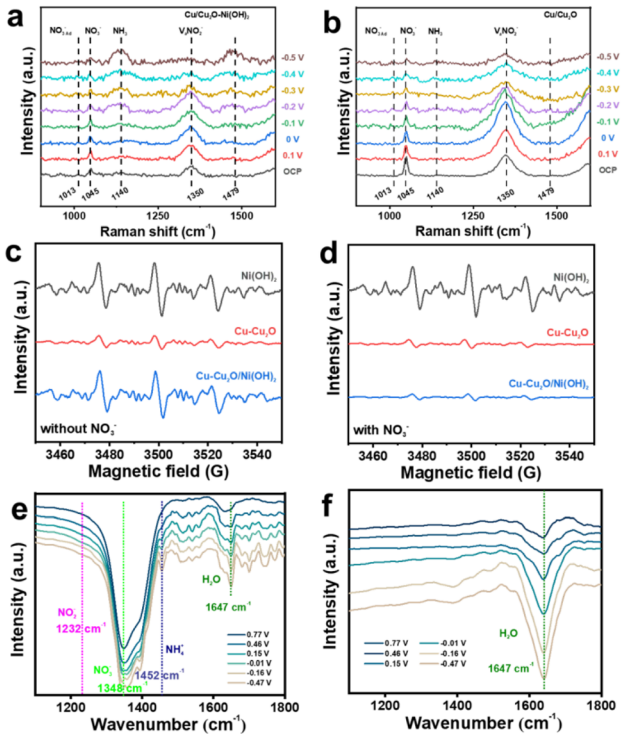

Fig. 7 *In situ* Measurements and EPR spectra of the electrocatalyst during the reaction. (a) *In situ* Raman spectra of Cu–Cu_2O/$Ni(OH)_2$ (a) and Cu–Cu_2O (b) during eNITRR at different potentials (V *vs.* RHE) in a mixed solution (0.1 M $NaNO_3$ + 0.1 M NaOH). EPR spectra of different materials without (c) and with (d) NO_3^-. *In situ* infrared spectra of Cu–Cu_2O/$Ni(OH)_2$ with (e) and without (f) NO_3^- at different potentials.

contribution from the reverse path is non-negligible. Additionally, if the generated H_2 is locally trapped inside the nanostructure of our catalyst, a worse result would be foreseen since it will suppress the HER process (*i.e.* the generation of *H). In either scenario, lower FE will be obtained.[40–43]

To more intuitively support the above hypothesis, we tracked the changes in the hydrogen generation effect of Cu–Cu_2O/$Ni(OH)_2$ and Cu–Cu_2O in the presence of NO_3^- over time using digital photos. As shown in Fig. 6d and e, for Cu–Cu_2O, visible bubbles can be seen within 4 min, while for Cu–Cu_2O/$Ni(OH)_2$, the same hydrogen generation effect as Cu–Cu_2O was observed more than 10 min later (Fig. 6d–f), indicating that the *H generated by $Ni(OH)_2$ activated H_2O was consumed by NO_2^- generated by Cu–Cu_2O catalyzed NO_3^-. It is preliminarily speculated that Cu–Cu_2O catalyzes the reduction of NO_3^- to NO_2^-, while $Ni(OH)_2$ catalyzes water to produce *H to further promote the hydrogenation reduction of NO_2^-.

In situ electrochemical Raman spectroscopy was used to investigate the process of reducing NO_3^- to NH_3 over Cu–Cu_2O/$Ni(OH)_2$ (Fig. 7a) and Cu–Cu_2O (Fig. 7b) catalysts in a mixed solution (0.1 M $NaNO_3$ + 0.1 M NaOH) within the potential range of 0.1 to −0.5 V (*vs.* RHE). At 0.1V, the Raman band at 1045 cm^{-1} was clearly observed on both Cu–Cu_2O/$Ni(OH)_2$ and Cu–Cu_2O catalysts, which can be attributed to the vibration mode of aqueous NO_3^-.[44] As the potential decreases and nitrate is continuously consumed in the aqueous solution, the intensity of the Raman band at 1045 cm^{-1} gradually diminishes. Correspondingly, the Raman band of adsorbed NO_3^- ($NO_3^-{}_{Ad}$) appears and gradually strengthens at 1013 cm^{-1}. At 0.1 V (*vs.* RHE), the Raman band of 1350 cm^{-1} is attributed to the stretching vibrations of NO_2^-,[45] and its intensity decreases with decreasing potential. It is evident that the reduction degree of the Raman band of NO_2^- in Cu–Cu_2O/$Ni(OH)_2$ is significantly higher than that in Cu–Cu_2O, indicating that Cu–Cu_2O/$Ni(OH)_2$ can greatly enhance water activation and promote the progressive hydrogenation process from NO_2^- to NH_3. The two Raman bands at 1140 cm^{-1} and 1479 cm^{-1} are attributed to ν (NH_3) and ν(antisymmetric NH_2 def. of NH_4^+) at 0.1 V,[46] and their strength gradually increases with decreasing potential. Additionally, the increase in these two bands' intensity in Cu–Cu_2O/$Ni(OH)_2$ is significantly higher than that in Cu–Cu_2O catalysts. The above results show that NO_2^- is quickly converted into NH_3 on Cu–Cu_2O/$Ni(OH)_2$ catalyst, indicating its high catalytic activity for the electrocatalytic reduction of NO_3^- to NH_3.

We used 5,5-dimethyl-1-pyrrolineN-oxide (DMPO) as the *H capture agent and examined the capability of $Ni(OH)_2$, Cu–Cu_2O, and Cu–Cu_2O/$Ni(OH)_2$ to produce active hydrogen in the absence of NO_3^- *via* EPR. As shown in Fig. 7c, the H-DMPO peak intensity for Cu–Cu_2O/$Ni(OH)_2$ is significantly higher than that of Cu–Cu_2O, but close to that of Ni $(OH)_2$, indicating that the introduction of $Ni(OH)_2$ improves the activation of the material for water. Subsequently, we probed whether the *H produced on the material was involved in the hydrogenation process of electrocatalytic nitrate reduction intermediates by monitoring the EPR spectrum of the electrolyte after introducing NO_3^- (Fig. 7d). In the presence of NO_3^-, little change was observed in the H-DMPO signals for $Ni(OH)_2$ and Cu–Cu_2O, while the H-DMPO signal for Cu–Cu_2O/$Ni(OH)_2$ was significantly attenuated. This result indicates that the *H generated on the Cu–Cu_2O/$Ni(OH)_2$ surface during the catalytic hydrogenation process is rapidly consumed by the nitrogen-containing intermediate species. Nevertheless, $Ni(OH)_2$ exhibits minimal activity in the electrocatalytic reduction of nitric acid, possibly attributed to its inadequate adsorption of nitric acid.

We utilized *in situ* Fourier transform infrared (FTIR) spectroscopy to investigate potential intermediates on the surfaces of $Ni(OH)_2$, Cu–Cu_2O, and Cu–Cu_2O/$Ni(OH)_2$ under different applied potentials. *Ex situ* infrared tests were conducted on standard samples (NO_3^-, NO_2^-, NH_4^+) to further monitor potential intermediates on these surfaces (Fig. S24–S26). The experimental findings revealed that in the presence of NO_3^-, distinct peaks corresponding to N–O stretching vibration of NO_3^-, N–H bending vibration of NH_4^+, and O–H bending vibration of H_2O appeared at 1348 cm^{-1}, 1452 cm^{-1}, and 1647 cm^{-1} Fig. 7e for Cu–Cu_2O/$Ni(OH)_2$ as the potential changed from 0.77 V to −0.47 V (*vs.*RHE).[47] Meanwhile, only peaks corresponding to the bending vibrations of NO_3^- and H_2O were observed in the $Ni(OH)_2$ system alone without detecting an NH_4^+ peak (Fig. S27, SI).[48] In the Cu–Cu_2O system (Fig. S28, SI), a peak at 1232 cm^{-1} attributed to N–O bending vibration of NO_2^- was clearly observed but was absent in the Cu–Cu_2O/$Ni(OH)_2$ catalytic system. This indicates that NO_2^- is further reduced and rapidly consumed in the Cu–Cu_2O/$Ni(OH)_2$

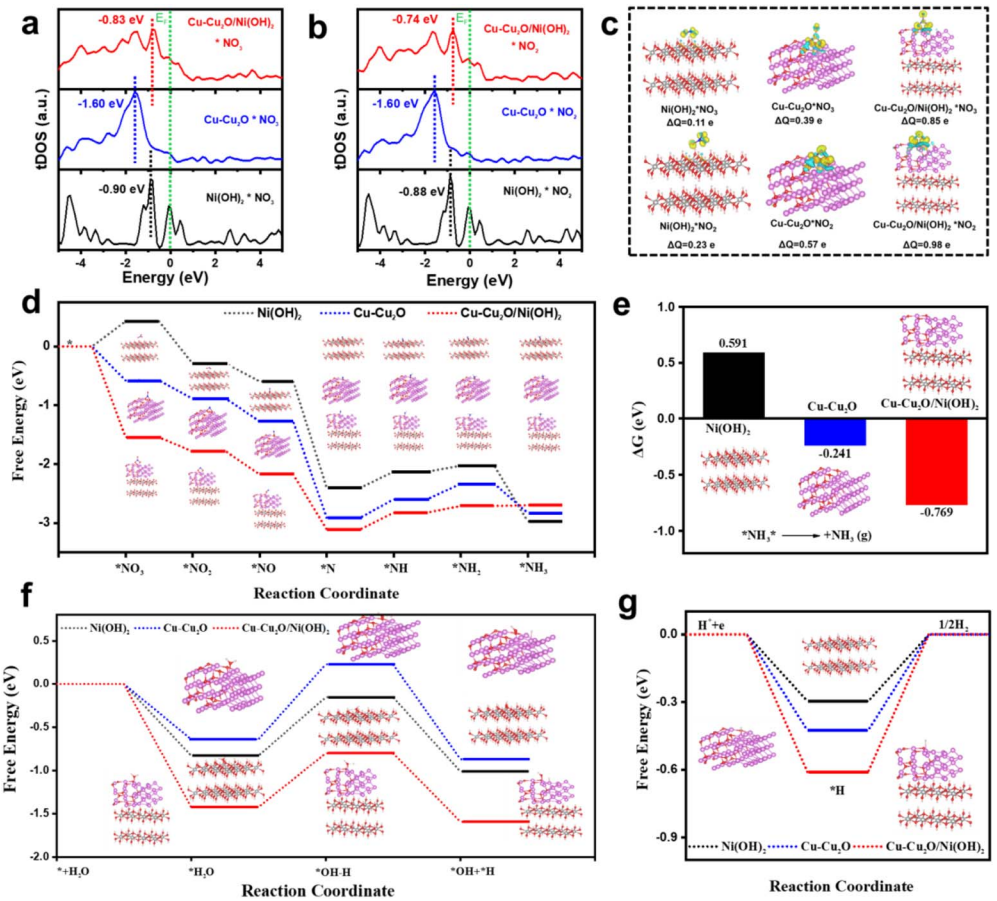

Fig. 8 DFT calculations elucidating the reaction mechanism and synergy. Total density of states of Cu–Cu_2O, $Ni(OH)_2$, and Cu–Cu_2O/$Ni(OH)_2$ after adsorption of (a) *NO_3 and (b) *NO_2, respectively. E_F denotes the Fermi level. The short-dashed lines with distinct colors are the position of the d-band center, respectively. (c) The differential charge density of the adsorption structure of Cu–Cu_2O, $Ni(OH)_2$ and Cu–Cu_2O/$Ni(OH)_2$ for NO_3^- and NO_2^- and the corresponding electron transfer number. The value of the isosurface is 0.002 e/Å^3. Yellow is the area where electrons accumulate and blue is the area where electrons dissipate. (d) Reaction free energies for different intermediates on a Cu–Cu_2O, $Ni(OH)_2$, and Cu–Cu_2O/$Ni(OH)_2$ catalyst surface. (e) The free energy change of NH_3 desorption on Cu–Cu_2O, $Ni(OH)_2$, and Cu–Cu_2O/$Ni(OH)_2$. (f) Free energy change of reaction for the activation of Cu–Cu_2O, $Ni(OH)_2$, and Cu–Cu_2O/$Ni(OH)_2$ for the production of *H on water. (g) Free energy change for the production of H_2 on Cu–Cu_2O, $Ni(OH)_2$ and Cu–Cu_2O/$Ni(OH)_2$.

catalytic system, consistent with the results shown in Fig. 6a. Additionally, time-resolved *in situ* infrared spectroscopy FTIR of isotope labeling experiments also clearly observed the N–H bending vibration of NH_4^+ at 1452 cm^{-1} (Fig. S29, SI). Fig. 7f showed a broad peak at approximately 1647 cm^{-1}, which is ascribed to δH_2O species in a solution without NO_3^-,[49] indicating the occurrence of water splitting in the solution. The above results suggest that in the electrocatalytic reduction of NO_3^- by Cu–Cu_2O/$Ni(OH)_2$, the Cu–Cu_2O site predominantly catalyzes the generation of NO_2^-, while the incorporation of $Ni(OH)_2$ site leads to a substantial production of *H, which synergistically enhances the formation of NH_3, resulting in outstanding electrocatalytic performance of Cu–Cu_2O/$Ni(OH)_2$ in nitrate reduction.

Theoretical validation of reaction pathways and synergistic effects

Density functional theory (DFT) calculations were performed to gain atomic-level insight into the enhanced eNITRR activity. The reliability and convergence of the DFT calculations were validated by systematically examining the U value, k-point sampling, cutoff energy, slab model construction (fixed layers indicated by dashed lines), and the convergence of total energy with respect to vacuum layer thickness (Fig. S30–S33, SI). Models for Cu–Cu_2O, $Ni(OH)_2$, and the Cu–Cu_2O/$Ni(OH)_2$ heterojunction were constructed (Fig. S34 and Table S3, SI). The calculated energies of different species on various catalysts are presented in Tables S4–S7. The calculated d-band centers (Fig. 8a and b) for Cu–Cu_2O/$Ni(OH)_2$ shifted closer to the Fermi level compared to the individual components, indicating optimized adsorption strength for NO_3^- and NO_2^- intermediates. Differential charge density analysis (Fig. 8c) revealed that the charge transfer from Cu–Cu_2O/$Ni(OH)_2$ to NO_3^- (0.85 e$^-$) and NO_2^- (0.98 e$^-$) was substantially greater than that from Cu–Cu_2O (0.39 e$^-$, 0.57 e$^-$) or $Ni(OH)_2$ (0.11 e$^-$, 0.23 e$^-$), confirming the heterojunction's superior ability to activate these species.[50]

According to previous reports, the electrochemical reaction coordinates of NO_3^- to NH_3 involve deoxidation and hydrogenation processes. Fig. 8d, S35 and S37 (SI) illustrate a full

eNITRR pathway in 0.1 M KOH (pH = 13) at 0 V *versus* Standard Hydrogen Electrode (SHE). For the adsorption of $*NO_3$, Cu–Cu_2O and Cu–Cu_2O/$Ni(OH)_2$ exhibit lower free energies (ΔG = −0.58 eV and ΔG = −1.55 eV), while $Ni(OH)_2$ demonstrates the highest free energy change (0.43 eV). On the Cu–Cu_2O surface, the potential-dependent reduction of *N to *NH step has the highest free energy change of 0.32 eV. In contrast to Cu–Cu_2O, the introduction of $Ni(OH)_2$ promotes the hydrogenation process (ΔG = +0.29 eV) of *N reduction to *NH. The findings indicate that Cu–Cu_2O/$Ni(OH)_2$ facilitates the adsorption of $*NO_3$ and the reduction of *N to *NH step. Compared with Cu–Cu_2O and $Ni(OH)_2$, Cu–Cu_2O/$Ni(OH)_2$ has a lower activation energy in the overall reaction path, which is more conducive to catalyzing the overall process of NO_3^- reduction to NH_3. In addition, Cu–Cu_2O/$Ni(OH)_2$ is more conducive to the desorption of NH_3, which is a thermodynamically favorable step (Fig. 8e).

For the eNITRR process, the activation of water to promote its gradual hydrogenation process is an important process to improve the performance of the catalyst. Therefore, we calculate the activation process of different catalysts to water (Fig. S37, SI). As shown in Fig. 8f and g, the Cu–Cu_2O catalyst necessitates a greater input of free energy change to activate water and generate *H, whereas the introduction of $Ni(OH)_2$, a catalyst that facilitates water activation, requires less free energy change to achieve the same effect. However, $Ni(OH)_2$ tends to bind with *H, leading to H_2 evolution and subsequent *H consumption, which hinders the progress of eNITRR. In contrast, the Cu–Cu_2O/$Ni(OH)_2$ catalyst exhibits lower free energy change for water activation to generate *H and demonstrates a higher free energy change in the subsequent combination of *H to form H_2. This indicates that the Cu–Cu_2O/$Ni(OH)_2$ catalyst is more probable than the other catalysts to utilize the generated *H to promote the eNITRR hydrogenation reduction process.

Conclusions

In summary, we have developed a widely applicable redox-potential-mediated strategy for the precise synthesis of 0D/2D Cu–Cu_2O/$MO_x(OH)_y$ (M = Ni, Fe, Mn, Co, Cr) heterojunctions. By leveraging the inherent differences in standard electrode potentials between Cu and transition metals M, we achieved selective oxidation and phase separation, resulting in the *in situ* formation of well-defined heterointerfaces with atomic-level precision. The more oxidizable M species are preferentially oxidized and hydrolyzed into ultrathin $MO_x(OH)_y$ nanosheets, while Cu undergoes controlled oxidation to form Cu–Cu_2O nanoparticles epitaxially anchored on the nanosheets. As a proof of concept, the Cu–Cu_2O/$Ni(OH)_2$ heterojunction exhibits exceptional electrocatalytic performance for the nitrate reduction reaction (eNITRR), achieving a Faradaic efficiency of 98.15% and an outstanding ammonia yield rate of 12,974.5 μg cm^{-2} h^{-1} at a low catalyst loading of 1 mg cm^{-2}, surpassing most reported catalysts. Integrated experimental and theoretical analyses reveal that the superior performance originates from synergistic interfacial effects: Cu–Cu_2O facilitates nitrate adsorption and activation, while $Ni(OH)_2$ efficiently cleaves H_2O to generate active *H species for the rapid hydrogenation of nitrogen intermediates. The catalyst also demonstrates remarkable stability over 140 hours of continuous operation. This work provides a generalizable synthesis strategy and deepens the understanding of interface engineering at the atomic scale, offering a powerful platform for designing advanced electrocatalysts for sustainable chemical synthesis and energy conversion.

Experimental

Materials

Copper(II) chloride dihydrate ($CuCl_2 \cdot 2H_2O$, AR), nickel chloride hexahydrate ($NiCl_2 \cdot 6H_2O$, AR), sodium nitrate ($NaNO_3$, AR), and anhydrous sodium sulfate (Na_2SO_4, AR) were obtained from Chron Chemicals LTD. Ethanol (AR), *n*-hexane (AR), and acetone (AR) were supplied by Lianlong Bohua (Tianjin) Pharmaceutical Chemistry Co., LTD. Sodium oleate (98.0%), isotopically labeled sodium nitrate-^{15} N, and Nafion aqueous solution (5.0 wt%) were purchased from Macklin. Carbon felt, used as the substrate, was acquired from Sinero Technology Co., LTD. Prior to use, the carbon felt was cleaned *via* sequential ultrasonic washing with isopropanol, ethanol, and deionized water.

Synthesis of Cu nanoparticles. The complex precursor of Cu was prepared by hydrothermal method, and then the Cu nanoparticles were reduced in organic solvent under the action of ligands. 0.171 g (0.1 M) $CuCl_2 \cdot 2H_2O$ was firstly added to 30 mL deionized water, then continually added 40 mL ethanol and 70 mL *n*-hexane. Then 1.218 g (0.4 M) sodium oleate was also added into the above solution, stirred and refluxed at 70 °C for 8 h. After the solution was cooled, the solution was divided into two layers. The precursor of Cu complex was obtained by washing the upper solution in the divided solution. 10 mL of the precursor solution of Cu complex was measured and added to the mixed solution of 50 mL ethanol and 50 mL *n*-hexane, and then the Cu nanoparticles were rapidly reduced under the reduction of $NaBH_4$ (50 mg). Finally, the solution was centrifuged, washed and dried to obtain the Cu nanoparticles.

Synthesis of Ni nanoparticles. The synthesis method of nickel nanoparticles is similar to the above method. 0.238 g (0.1 M) $NiCl_2 \cdot 6H_2O$ was firstly added to 30 mL deionized water, then continually added 40 mL ethanol and 70 mL *n*-hexane. Then 1.218 g (0.4 M) sodium oleate was also added into the above solution, stirred and refluxed at 70 °C for 8 h. After the solution was cooled, the solution was divided into two layers. The precursor of Ni complex was obtained by washing the upper solution in the divided solution. 10 mL of the precursor solution of Ni complex was measured and added to the mixed solution of 50 mL ethanol and 50 mL *n*-hexane, and then the Ni nanoparticles were rapidly reduced under the reduction of $NaBH_4$ (50 mg). Finally, the solution was centrifuged, washed and dried to obtain the Ni nanoparticles.

Synthesis of CuNi nanoparticles. Take the precursor solution prepared above, 5 mL of the precursor solution of Ni complex and 5 mL of the precursor solution of Cu complex were measured and added to the mixed solution of 50 mL ethanol

and 50 mL *n*-hexane, and then the CuNi nanoparticles were rapidly reduced under the reduction of $NaBH_4$ (50 mg). Finally, the solution was centrifuged, washed and dried to obtain the CuNi nanoparticles.

Synthesis of Cu/Cu_2O nanoparticles. The prepared Cu nanoparticles were weighed 10 mg and added to 10 mL deionized water, and ultrasounded at 35 °C for 4 h. After ultrasound, the surface of Cu nanoparticles was partially oxidized to form Cu–Cu_2O nanoparticles. Finally, the solution after ultrasound is centrifuged, washed and dried to obtain Cu–Cu_2O nanoparticles.

Synthesis of $Ni(OH)_2$ nanosheets. The prepared Ni nanoparticles were weighed 10 mg and added to 10 mL deionized water and ultrasounded at 35 °C for 4 h. Due to hydrolysis, Ni nanoparticles were gradually hydrolyzed into $Ni(OH)_2$ nanosheets. Finally, the ultrasonic solution was centrifuged, washed and dried to obtain $Ni(OH)_2$ nanosheets.

Synthesis of Cu–Cu_2O/$Ni(OH)_2$ nanosheets. The prepared CuNi nanoparticles were weighed at 10 mg and added to 10 mL of deionized water and ultrasounded at 35 °C for 4 h. Due to hydrolysis, CuNi nanoparticles formed $Ni(OH)_2$ nanosheets *in situ* and loaded Cu–Cu_2O nanoparticles at the same time. Finally, the ultrasonic solution was centrifuged, washed and dried to obtain Cu–Cu_2O/$Ni(OH)_2$ nanosheets.

Electrocatalytic performance measurements. The electrocatalytic activity measurements were performed in an open two-compartment H-cell separated. Electrode preparation: 1 milligram of the catalyst were ultrasonically dispersed in a mixed solution 0.95 mL of isopropyl alcohol and 50 μL of Nafion solution (5 wt%). All of the dispersed catalyst slurry was dropped onto 1 cm^2 of carbon felt (Except for the specified conditions) as the work electrode, followed by drying at 60 °C for 4 h. A Platinum tablet (1*1 cm^2) and a SCE (filled with saturated KCl) were used as counter and reference electrodes, respectively. The 30 mL NaOH (0.1 M) solution was used as the anodic electrolyte and the 30 mL NaOH (0.1 M)/$NaNO_3$–N (500 mg L^{-1}) solution was used as the cathodic electrolyte. The electrolyte in the cathodic compartment was stirred at a rate of 200 rpm during electrolysis in a 28 °C water bath. All of the electrocatalytic nitrate reduction reaction (eNITRR) experiments were performed using a three-electrode system connected to an electrochemical workstation (CHI 760E). The pH is 13.0 in this mixing electrolyte system. All potentials measured were calibrated to *vs.* RHE (reversible hydrogen electrode) using the following formula.

$$E\,(\mathrm{RHE}) = E\,(\mathrm{SHE}) + 0.0592 \times \mathrm{pH} + 0.24$$

ECSA measurements. The cycle voltammetry profiles were obtained using a glassy carbon electrode (GCE, 0.071 cm^2) deposited 10 μL catalyst ink as the working electrode. The catalyst ink formula: 10 mg of the catalyst was ultrasonically dispersed in a mixed solution 0.95 mL of isopropyl alcohol and 50 μL of Nafion solution (5 wt%).

$^{15}NO_3^-$ isotope labeling experiments quantification by 1H NMR. ^{1}H NMR spectroscopy (400 MHz) was used to detect ammonia in the isotope-labelling measurement. The generated NH_3 was collected in the HCl solution. Next, all of the sample solutions were rotary evaporated to remove water and excess HCl, a white powder sample was obtained. Then, the power sample was mixed with 5 mg maleic acid ($C_4H_4O_4$, internal standard) and dissolved in 0.5 mL DMSO-d6 (hexadeuterodimethyl sulfoxide). Finally, the prepared mixture was tested by a JNM-ECS 400 M spectrometer at ambient conditions and the NH_3 product peaks were analyzed.

Author contributions

Tuo Zhang: data curation, formal analysis, investigation methodology, software, writing – original draft; Tianzhi Hao: data curation, formal analysis, investigation, methodology, writing – original draft; Xiangyang Hou: software, writing – original draft, Yuhui Yin: data curation, investigation, methodology, software, writing – original draft; Guowen Hu: data curation, investigation, methodology, writing – original draft; Genping Meng: data curation, investigation, methodology, software, writing – original draft; Shihao Sun: data curation, investigation, methodology, software, writing – original draft; Hua Li: data curation, investigation, methodology, software, writing – original draft; Baodui Wang: conceptualization, formal analysis, investigation, methodology, resources, funding acquisition, supervision, project administration, and writing – review & editing.

Conflicts of interest

There are no conflicts to declare.

Data availability

All the data supporting this article have been included in the main text and the supplementary information (SI). Supplementary information is available. See DOI: https://doi.org/10.1039/d5sc08998k.

Acknowledgements

The work was financially supported by the National Natural Science Foundation of China (22377047, 22221001), Science and Technology Leading Talent Foundation of Gansu Province (24RCKB003).

Notes and references

1 Y. Yin and A. P. Alivisatos, *Nature*, 2005, **437**, 664–670.
2 X. Huang, Z. Zeng and H. Zhang, *Chem. Soc. Rev.*, 2013, **42**, 1934–1946.
3 H. Jia, Y. Wang, Y. Yang, C. Liu and W. He, *RSC Adv.*, 2025, **15**, 40056–40066.
4 C. Zhu, T. Gong, Q. Xian and J. Xie, *Appl. Surf. Sci.*, 2018, **444**, 75–86.
5 B. Shang, X. Cui, L. Jiao, K. Qi, Y. Wang, J. Fan, Y. Yue, H. Wang, Q. Bao, X. Fan, S. Wei, W. Song, Z. Cheng, S. Guo and W. Zheng, *Nano Lett.*, 2019, **19**, 2758–2764.

6 Z. Wang, H. Guo, S. Shao, M. Saghayezhian, J. Li, R. Fittipaldi, A. Vecchione, P. Siwakoti, Y. Zhu, J. Zhang and E. W. Plummer, *Proc. Natl. Acad. Sci. U. S. A.*, 2018, **115**, 9485–9490.
7 H. Xu, Y. Ma, J. Chen, W.-x. Zhang and J. Yang, *Chem. Soc. Rev.*, 2022, **51**, 2710–2758.
8 Z. Mei, Y. Zhou, W. Lv, S. Tong, X. Yang, L. Chen and N. Zhang, *ACS Sustain. Chem. Eng.*, 2022, **10**, 12477–12496.
9 Y. Lei, L. Zhang, X. Wang, D. Wang, Y. Zhao, B. Zhang, N. Zhang and H. Shang, *Chem. Sci.*, 2025, **16**, 18298–18308.
10 B. Zhou, Y. Tong, Y. Yao, W. Zhang, G. Zhan, Q. Zheng, W. Hou, X.-K. Gu and L. Zhang, *Proc. Natl. Acad. Sci. U. S. A.*, 2024, **121**, e2405236121.
11 J. Geng and S. Ji, *Nano Res.*, 2024, **17**, 4898–4907.
12 Y. Wang, Z. Bai, K. Huang, S. Wang, F. Wang and M. Wu, *J. Mater. Chem. A*, 2025, **13**, 12226–12233.
13 Y. Qu, T. Dai, Y. Cui, G. Ding, Y. Zhu, Z. Wang and Q. Jiang, *Small*, 2024, **20**, 2308246.
14 Y. Zhou, R. Duan, H. Li, M. Zhao, C. Ding and C. Li, *ACS Catal.*, 2023, **13**, 10846–10854.
15 D. Guo, X.-X. Xue, M. Jiao, J. Liu, T. Wu, X. Ma, D. Lu, R. Zhang, S. Zhang, G. Shao and Z. Zhou, *Chem. Sci.*, 2024, **15**, 16281–16290.
16 X. Zhang, X. Liu, Z.-F. Huang, L. Gan, S. Zhang, R. Jia, M. Ajmal, L. Pan, C. Shi, X. Zhang, G. Yang and J.-J. Zou, *Energy Environ. Sci.*, 2024, **17**, 6717–6727.
17 J. Yu, Z. Xi, J. Su, P. Jing, X. Xu, B. Liu, Y. Wang and J. Zhang, *eScience*, 2025, **5**, 100350.
18 W. Zhang, Y. Yao, Z. Chen, S. Zhao, F. Guo and L. Zhang, *Environ. Sci. Technol.*, 2024, **58**, 7208–7216.
19 F.-Y. Chen, Z.-Y. Wu, S. Gupta, D. J. Rivera, S. V. Lambeets, S. Pecaut, J. Y. T. Kim, P. Zhu, Y. Z. Finfrock, D. M. Meira, G. King, G. Gao, W. Xu, D. A. Cullen, H. Zhou, Y. Han, D. E. Perea, C. L. Muhich and H. Wang, *Nat. Nanotechnol.*, 2022, **17**, 759–767.
20 Y. Wan, M. Pei, Y. Tang, Y. Liu, W. Yan, J. Zhang and R. Lv, *Adv. Mater.*, 2025, **37**, 2417696.
21 X. Wu, J. Lin, Y. Zhang, R.-C. Sun and Z.-S. Wu, *ACS Catal.*, 2025, **15**, 15640–15648.
22 K. Wang, L. Zhang, Y. Su, D. Shao, S. Zeng and W. Wang, *J. Mater. Chem. A*, 2018, **6**, 8366–8373.
23 Z. Zhu, H. Yin, C.-T. He, M. Al-Mamun, P. Liu, L. Jiang, Y. Zhao, Y. Wang, H.-G. Yang, Z. Tang, D. Wang, X.-M. Chen and H. Zhao, *Adv. Mater.*, 2018, **30**, 1801171.
24 H. Zhang, *ACS Nano*, 2015, **9**, 9451–9469.
25 Y. Zhang, Y. Liu, Y. Wang, P. G. Schultz and F. Wang, *J. Am. Chem. Soc.*, 2015, **137**, 38–41.
26 O. Antonoglou, K. Lafazanis, S. Mourdikoudis, G. Vourlias, T. Lialiaris, A. Pantazaki and C. Dendrinou-Samara, *Mater Sci Eng C*, 2019, **99**, 264–274.
27 C. Liu and Y. Li, *J. Alloys Compd.*, 2009, **478**, 415–418.
28 T. Ren, Z. Yu, H. Yu, K. Deng, Z. Wang, X. Li, H. Wang, L. Wang and Y. Xu, *Appl. Catal., B*, 2022, **318**, 121805.
29 J. A. Torres-Ochoa, D. Cabrera-German, O. Cortazar-Martinez, M. Bravo-Sanchez, G. Gomez-Sosa and A. Herrera-Gomez, *Appl. Surf. Sci.*, 2023, **622**, 156960.
30 Y. Kim, J. Ko, M. Shim, J. Park, H. H. Shin, Z. H. Kim, Y. Jung and H. R. Byon, *Chem. Sci.*, 2024, **15**, 2578–2585.
31 J. Zhou, M. Wen, R. Huang, Q. Wu, Y. Luo, Y. Tian, G. Wei and Y. Fu, *Energy Environ. Sci.*, 2023, **16**, 2611–2620.
32 Z. Fu, J. Hu, W. Hu, S. Yang and Y. Luo, *Appl. Surf. Sci.*, 2018, **441**, 1048–1056.
33 F. Zhang, Z. Liu, X. Chen, N. Rui, L. E. Betancourt, L. Lin, W. Xu, C.-j. Sun, A. M. M. Abeykoon, J. A. Rodriguez, J. Teržan, K. Lorber, P. Djinović and S. D. Senanayake, *ACS Catal.*, 2020, **10**, 3274–3284.
34 W.-H. Pi, Q.-J. Li, M. Wu, Y.-Z. Huang, X.-L. Deng, L. Huang, L.-B. Jiang and H.-X. Zhang, *Appl. Surf. Sci.*, 2019, **493**, 185–192.
35 H. Luo, S. Li, Z. Wu, M. Jiang, M. Kuang, Y. Liu, W. Luo, D. Zhang and J. Yang, *Adv. Funct. Mater.*, 2024, **34**, 2403838.
36 S. Han, H. Li, T. Li, F. Chen, R. Yang, Y. Yu and B. Zhang, *Nat. Catal.*, 2023, **6**, 402–414.
37 Y. Bu, C. Wang, W. Zhang, X. Yang, J. Ding and G. Gao, *Angew Chem. Int. Ed. Engl.*, 2023, **62**, e202217337.
38 C. Wan, Z. Zhang, J. Dong, M. Xu, H. Pu, D. Baumann, Z. Lin, S. Wang, J. Huang, A. H. Shah, X. Pan, T. Hu, A. N. Alexandrova, Y. Huang and X. Duan, *Nat. Mater.*, 2023, **22**, 1022–1029.
39 Z. Wang, S. Liu, X. Zhao, M. Wang, L. Zhang, T. Qian, J. Xiong, C. Yang and C. Yan, *ACS Mater. Lett.*, 2023, **5**, 1018–1026.
40 X. Mu, X. Zhang, Z. Chen, Y. Gao, M. Yu, D. Chen, H. Pan, S. Liu, D. Wang and S. Mu, *Nano Lett.*, 2024, **24**, 1015–1023.
41 C. Wan, Y. Ling, S. Wang, H. Pu, Y. Huang and X. Duan, *ACS Cent. Sci.*, 2024, **10**, 658–665.
42 W. Liang, X. Gong, J. Xu, Z. Dan, F. Xie, H. Yu, H.-F. Wang, Y. Jin, H. Wang, Y. Cao, H. Meng and H. Yu, *J. Energy Chem.*, 2024, **95**, 529–539.
43 Y. Huang, X. Li, P. K. Shen, C. Yang and J. Zhu, *ACS Mater. Lett.*, 2024, **6**, 1678–1685.
44 N. Sergent, M. Epifani and T. Pagnier, *J. Raman Spectrosc.*, 2006, **37**, 1272–1277.
45 Y. Liu, J. Ma, S. Huang, S. Niu and S. Gao, *Nano Energy*, 2023, **117**, 108840.
46 A. B. Phatangare, S. S. Dahiwale, S. D. Dhole and V. N. Bhoraskar, *Radiat. Phys. Chem.*, 2023, **204**, 110704.
47 K. Fan, W. Xie, J. Li, Y. Sun, P. Xu, Y. Tang, Z. Li and M. Shao, *Nat. Commun.*, 2022, **13**, 7958.
48 J. Li, H. Li, K. Fan, J. Y. Lee, W. Xie and M. Shao, *Chem Catal.*, 2023, **3**, 100638.
49 S. Liu, T. Qian, M. Wang, H. Ji, X. Shen, C. Wang and C. Yan, *Nat. Catal.*, 2021, **4**, 322–331.
50 H. Niu, Z. Zhang, X. Wang, X. Wan, C. Shao and Y. Guo, *Adv. Funct. Mater.*, 2020, **31**, 2008533.